Quantitative X-ray Scattering of Free Molecules

Lingyu Ma¹, Nathan Goff¹, Andrés Moreno Carrascosa², Silke Nelson³, Mengning Liang³, Xinxin Cheng³, Haiwang Yong⁴, Ian Gabalski⁵,⁶, Lisa Huang¹, Stuart W. Crane¹, Alice E. Green⁶, ⁷, Felix Allum³,⁶, Philipp Lenzen⁶, Sri Bhavya Muvva⁶, Lauren F. Heald⁶, Yusong Liu³, Surjendu Bhattacharyya³, Kirk A. Larsen³, Martin Graßl³,⁶, Ruaridh Forbes³, Martin Centurion⁶, Thomas J. A. Wolf³,⁶, Adam Kirrander², Michael P. Minitti³, and Peter M. Weber¹*

Abstract

Advances in X-ray free electron lasers have made ultrafast scattering a powerful method for investigating molecular reaction kinetics and dynamics. Accurate measurement of the ground-state, static scattering signals of the reacting molecules is pivotal for these pump-probe X-ray scattering experiments as they are the cornerstone for interpreting the observed structural dynamics. This article presents a data calibration procedure, designed for gas-phase X-ray scattering experiments conducted at the Linac Coherent Light Source X-ray Free-Electron Laser at SLAC National Accelerator Laboratory, that makes it possible to derive a quantitative dependence of the scattering signal on the scattering vector. A self-calibration algorithm that optimizes the detector position without reference to a computed pattern is introduced. Angle-of-scattering corrections that account for several small experimental non-idealities are reported. Their implementation leads to near quantitative agreement with theoretical scattering patterns calculated with *ab-initio* methods as illustrated for two X-ray photon energies and several molecular test systems.

1. Introduction

The identification and characterization of structures and electron density distributions of static and reacting molecules with high accuracy are at the core of chemistry and related molecular sciences^{1,2,3}. Advancements in pump-probe spectroscopy techniques using ultrafast lasers have enabled the real-time monitoring of chemical reactions by tracking the temporal spectrum

¹Department of Chemistry, Brown University, Providence, RI, USA

²Physical and Theoretical Chemistry Laboratory, Department of Chemistry, University of Oxford, Oxford, UK

³Linac Coherent Light Source, SLAC National Accelerator Laboratory, Menlo Park, CA, USA

⁴Department of Chemistry and Biochemistry, University of California, San Diego, CA, USA

⁵Department of Applied Physics, Stanford University, Stanford, CA, USA.

⁶Stanford PULSE Institute, SLAC National Accelerator Laboratory, Menlo Park, CA, USA

⁷European XFEL, 22869 Schenefeld, Germany

⁸Department of Physics and Astronomy, University of Nebraska-Lincoln, Lincoln, NE, USA

^{*} Correspondence to: peter weber@brown.edu (P.M.W.)

evolution of the reacting molecules^{4,5,6,7,8,9,10,11}. More recently, ultrafast scattering experiments have greatly enhanced the experimental arsenal and provided new structural views of fundamental chemical processes^{12,13,14}.

Although ultrafast spectroscopies provide important insights into electronic and vibrational states as well as their time evolution, these spectroscopies only offer indirect probes of the molecular structures, even in favorable cases. 15,16,17,18,19,20,21 In contrast, scattering measurements directly reflect electron densities and interatomic distances within the molecule. With the development of technologies capable of generating ultrafast pulses, initially on electron beams 22,23,24,25,26, a new era has emerged where molecular systems in transient excited states may be measured 27,28,29,30,31,32,33,34. Recently, the introduction of X-ray Free Electron Lasers (XFEL) and Mega-electron-Volt radiofrequency (RF) electron guns has revolutionized the field. 35,36,37 These advances enable the determination of transient molecular structures with sub-Ångstrom spatial resolution and femtosecond time resolution, even in small organic molecules 38,39. Moreover, the development of high brightness XFELs has allowed for the study of photochemistry in low-density gas phase vapors, isolating molecular motions without the interference from nearby molecules as the reaction dynamics unfold.

X-ray scattering of free molecules in the gas-phase is uniquely positioned to advance research in molecular dynamics because the signals are purely intrinsic to the target molecule. This stands in contrast to ordered solid materials, where the intensity of Bragg peaks depends on the coherence of the X-rays and is affected by lattice defects and impurities. Additionally, while spectroscopic measurements depend on optical transitions, with often unknown cross sections, X-ray scattering intensities are only dependent on the number of electrons in a molecule and their relative arrangements with respect to each other. As a result, the intensities of X-ray scattering signals of different reaction transients are quantitatively related. A closely related scattering technique, electron diffraction, features the same conceptual advantages. However, it is encumbered by the overwhelming angular dependence of the Rutherford scattering cross section that makes experiments difficult to interpret quantitatively.³³ The quantitative nature of X-ray scattering, combined with the possibility to implement it in ultrafast pump-probe experiments, has led to important applications including the determinations of the electron density distribution and the nuclear structures of electronically excited states 40,41,42, measurement of coherent vibrational motion^{43,44,45}, monitoring of photodissociation reactions^{46,47}, imaging of electrocyclic reactions^{38,39}, and measurement of the dynamics and kinetics of various other molecular systems^{48,49,50}.

The measurement of pump-probe X-ray scattering signals benefits tremendously from analyzing the patterns as a percent difference ($P_{\rm diff}$), where excited state signals are related to the unexcited, ground-state static scattering signal^{27,49,50}

$$P_{\text{diff}}(\phi, q, t) = 100 \cdot \frac{I_{\text{on}}(\phi, q, t) - I_{0}(q)}{I_{0}(q)}$$
 Eq. 1.1

where $I_{\rm on}(\phi, q, t)$ is the scattering signal measured following excitation by the optical pump laser at delay time t, and $I_0(q)$ is the ground-state static scattering pattern of the reactant molecule without the optical pump. Representing the measured signals as a percent difference not only highlights the subtle changes in the scattering pattern over time, but more importantly, also cancels common experimental artifacts present equally in both the laser-on and laser-off signals. Examples

include the magnitude of scattering intensity as a function of q due to the diffractometer's internal shape, or slight instabilities in the gas pressure.

Yet analyzing pump-probe patterns in terms of the percentage difference signal implicitly assumes that the scattering pattern of the reactant, $I_0(q)$, is known and correctly measured. Any deviation of the measured pattern from its correct form carries through to the structures of excited states determined in the pump probe experiment. That is, excited state structures can only be determined to the extent that the ground state is known. An incorrect reference signal results in an erroneous determination of the excited-state molecular structure, molecular motions, and reaction pathways. This motivates the effort to quantitatively account for shortcomings inherent in the experiment. In addition, because X-ray scattering is directly related to the Fourier transform of the one and two electron densities in a molecule^{51,52,53}, accurate measurements of static X-ray scattering patterns can provide benchmarks for electronic structure theory and create experimental maps of molecular electron density distributions.

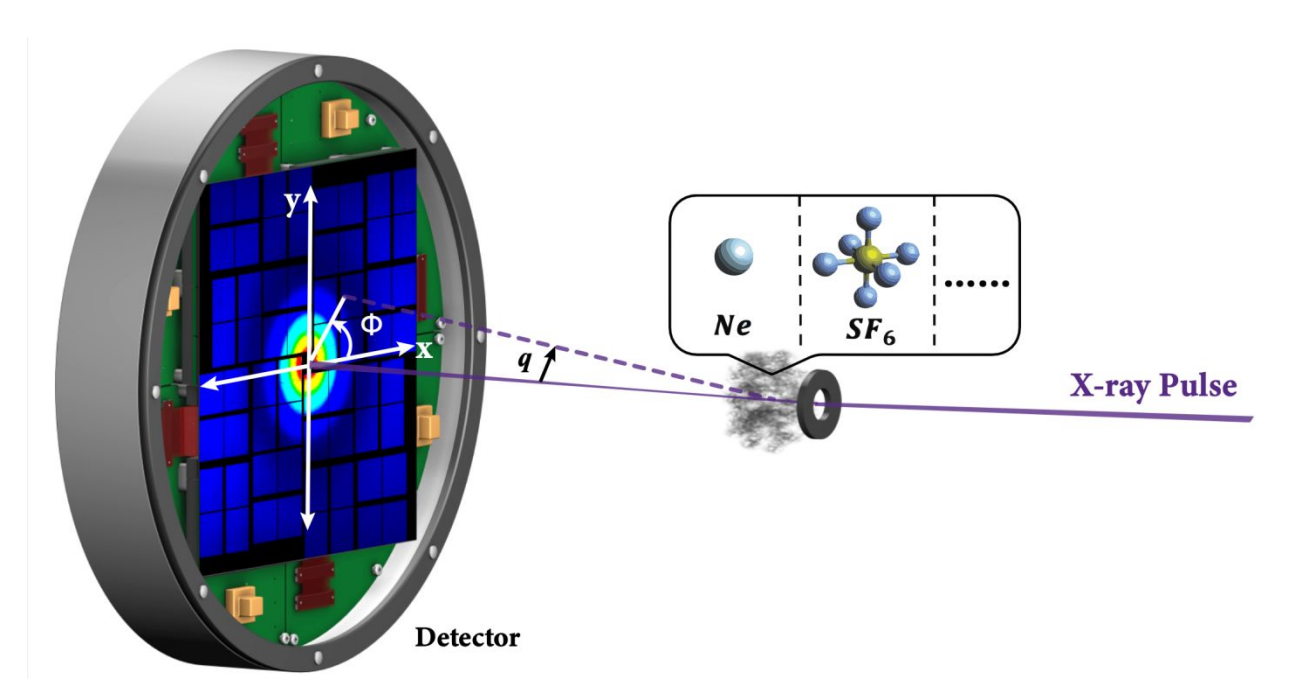


Figure 1: Experimental setup for static X-ray scattering. The static X-ray scattering pattern is created by the interaction of the intense X-ray beam with the dilute gas-phase molecules in the sample cell. The scattering signals are recorded as a function of the amplitude of the scattering vector \mathbf{q} and azimuthal angle $\mathbf{\phi}$.

In this article, we discuss corrections that need to be incorporated in a quantitative analysis of gasphase X-ray scattering experiments performed at the Linac Coherent Light Source (LCLS) at the SLAC National Accelerator Laboratory. The experimental layout, which has been described previously, involves an intense X-ray beam from the LCLS XFEL at SLAC National Accelerator Laboratory, Figure 1. The beam passes through a few millimeters of a low-pressure gas sample which scatters a small fraction of the X-rays. An area pixel detector measures the solid angle-dependent scattering, and its radial or azimuthal profile is analyzed for the molecular nuclear structure or the electron density. The implementation and data analysis of the ultrafast gas-phase

X-ray scattering experiments at LCLS have previously been discussed. 14,54 Since then, higher Xray photon energies have been used to study various molecular systems, and advances have been made in the analysis of experimental data. We introduce here a self-calibration algorithm for measuring the physical detector position from only the experimental pattern based on the polarization of the X-rays, eliminating the need to rely on theoretically simulated patterns. To achieve a quantitative agreement between experimental measurement and theoretical calculations, various angle-of-scattering corrections are introduced; these include corrections for angledependent scattering length and gas density associated with flow out of the scattering cell, absorption losses as a consequence of transmission through a beryllium window with a central hole, as well as thin aluminum and Kapton layers situated above the 2D X-ray detector, and underdetection corrections as a result of transmission through the silicon pixels of the detector. We also investigate approaches to further improve the data quality of the experiments and eliminate effects from unidentified instrumental errors. The resulting data calibration procedure leads to a precise characterization of static gas-phase X-ray scattering patterns over a wide range of X-ray photon energies. Excellent agreement between experimental measurements and high-level theoretical calculations have been achieved.

2. Methods

In order to thoroughly calibrate the absolute X-ray scattering signals measured with the Coherent X-ray Imaging (CXI) instrument at the LCLS (beamtime LW11 and L10160), it is necessary to consider the physical geometry of the detector relative to the interaction region, the polarization of the X-ray beam originating from the XFEL, and the design and components of the scattering cell. The scattering cell is windowless to avoid scattering of the intense primary X-ray beam by any window material. It is constructed of stainless steel with a 3.2 mm inlet tube for the gaseous target molecules, which are crossed by the X-rays for a pathlength of L = 2.4 mm. On the entrance side, the opening is made of a radius of 125 µm platinum aperture to block stray radiation and define the X-ray beam position. On the exit side, a radius of 250 µm hole in the beryllium window transmits the primary X-ray beam. These hole sizes were carefully chosen to avoid obstruction of the primary X-ray beam while allowing for sufficient gas flow between consecutive X-ray pulses. The details about the scattering cell design can be found in Ref. 14. The scattering signal is then detected on a 4-megapixel detector (Jungfrau 4M) which has 318.5 µm thick silicon pixels, topped with 3.5 µm thick aluminum coating. The Jungfrau 4M detector is further protected by a shield of 8 um Kapton NH covered with 1 um sputtered aluminum. The position of the detected X-rays is expressed in terms of the scattering vector q and the azimuthal angle ϕ . The ~30 fs X-ray pulses are weakly focused into the gas, keeping the intensity low enough to minimize any effects from ionization. The gas flow is sufficient that molecules exposed to an X-ray pulse have left the gas cell before the next pulse arrives. The pressure of the gas at the interaction region is intentionally kept low (~8 Torr), so that the pressure in the vacuum chamber outside the gas cell remains < 10⁻⁴ Torr. This minimizes unwanted scattering of background gas molecules outside of the sample cell.

A schematic of the X-ray scattering experimental setup is shown in Figure 2. Accurate calibration requires determination of the exact distance between the detector and sample, accounting for the attenuation of the scattered radiation by the beryllium window, the aluminum coating, and the Kapton NH/Al protective shield, consideration of the angle sensitivity of the detector, and a simulation of the gas streaming out of either side of the gas cell.

The method for the calculation of total scattering from *ab initio* electronic wave functions is based on previously developed code for the prediction of elastic^{55,56,57} and inelastic scattering⁵⁸. The wavefunctions used to obtain scattering cross sections are calculated using multireference configuration interaction (MRCI) with the choice of active space and basis specified in each case. The orientation of the molecules is isotropic for thermal liquids and gases, in which case the directional dependence of q is lost, and the signal must be rotationally averaged. The rotational averaging of the wavefunction is done numerically. The one- and two-particle density matrices are constructed from *ab initio* MRCI outputs considering both diagonal and off-diagonal terms. We use the electronic structure package MOLPRO⁵⁹ and a modified version of the *ab initio* X-ray diffraction (AIXRD)^{55,58} code to calculate the total scattering pattern.

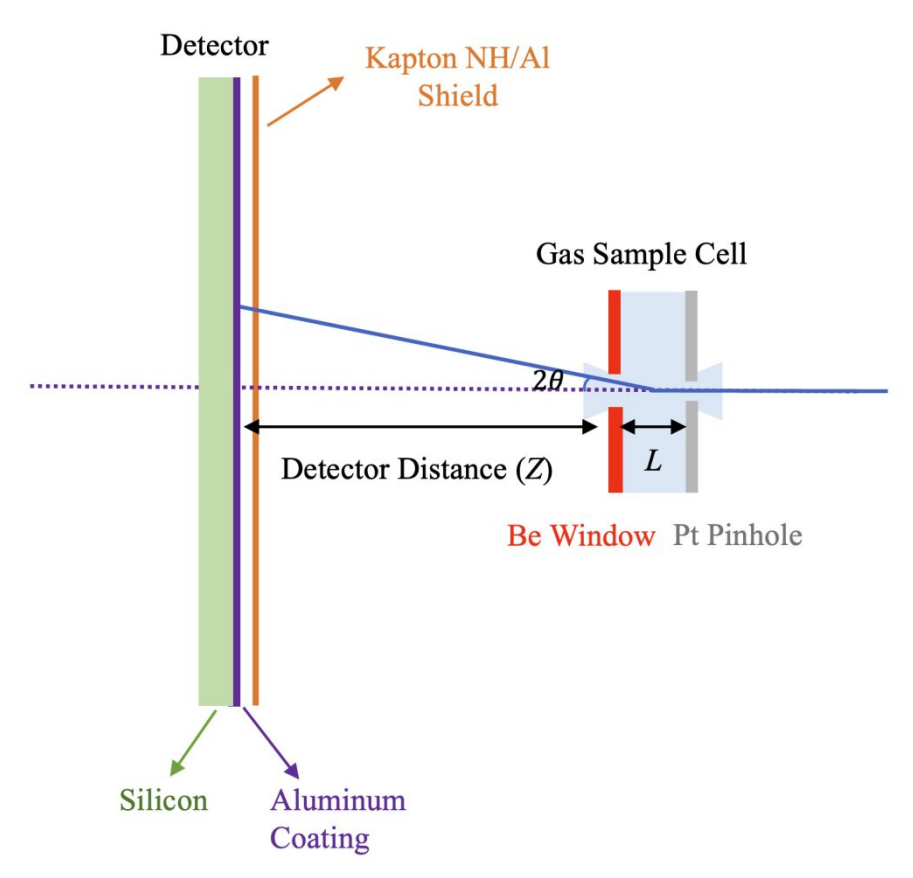


Figure 2: A schematic of the X-ray scattering experimental setup.

3. Corrections

3.1 Detector position calibration

In many X-ray scattering studies, the detector position is determined by comparing an experimental pattern of a well-known gas (typically SF₆) to a computationally modeled scattering pattern. This may produce satisfactory results, assuming high-level computations are used for the reference model. Employing simpler models, such as the commonly used independent atom model

(IAM), results in systematic deficiencies of the derived molecular structures⁶⁰. Additionally, using a computed pattern of a reference gas is conceptually wanting, as it merely shifts the need to calculate the scattering pattern from a reacting molecule of interest to some calibration molecule. It would be preferable to have a direct, experiment-only, method to calibrate the detector position.

Independent of the nature of an atom or the structure of a molecule, X-ray scattering depends on the polarization of the X-rays. For a linearly polarized X-ray beam, the intensity of elastic scattering by a free electron is⁶¹:

$$I_{\text{scatt}}(2\theta, \phi) = r_0^2 \cdot \frac{I_0}{Z^2} \cdot (\sin^2(\phi) + \cos^2(\phi) \cdot \cos^2(2\theta))$$
 Eq. 3.1.1

where I_0 and I_{scatt} are the incoming and scattered intensities, Z is the distance to the detector, and r_0 is the classic electron radius. The scattering angle 2θ is related to the transferred momentum vector \vec{q} where $|\vec{q}| = q = \frac{4\pi}{\lambda} sin\theta$. Scattering signals calculated from classic Thomson scattering equations express the scattering per unit area as a function of 2θ at a distance Z between the scattering medium and the point of detection. In the experiments, a planar detector is usually positioned perpendicular to the primary X-ray beam axis so that the distance Z depends on the scattering angle. Geometric correction factors must be applied for direct comparison to the calculated scattering patterns. Specifically, the measured scattering intensity should be divided by a $cos^2(2\theta)$ factor to correct for the Z dependence arising from the scattering per unit area. To normalize the effective area of pixels at different displacements from the beam axis, the measured scattering intensity should be further divided by an additional $cos(2\theta)$ factor. Combined, the measured scattered intensity is divided by $cos^3(2\theta)$ to compare with calculated theoretical scattering patterns¹⁴.

The X-rays produced by LCLS are linearly polarized, giving rise to a polarization factor sin^2 $(\phi) + cos^2(\phi) \cdot cos^2(2\theta)$ that depends on the scattering angle 2θ and the azimuthal angle with respect to the X-ray polarization, ϕ .⁵⁴ By applying both geometric and polarization correction factors to the measured scattering intensity while varying the detector position, the measured two-dimensional images can be used to derive the precise distance of the detector relative to the interaction region and its displacement from the beam axis.

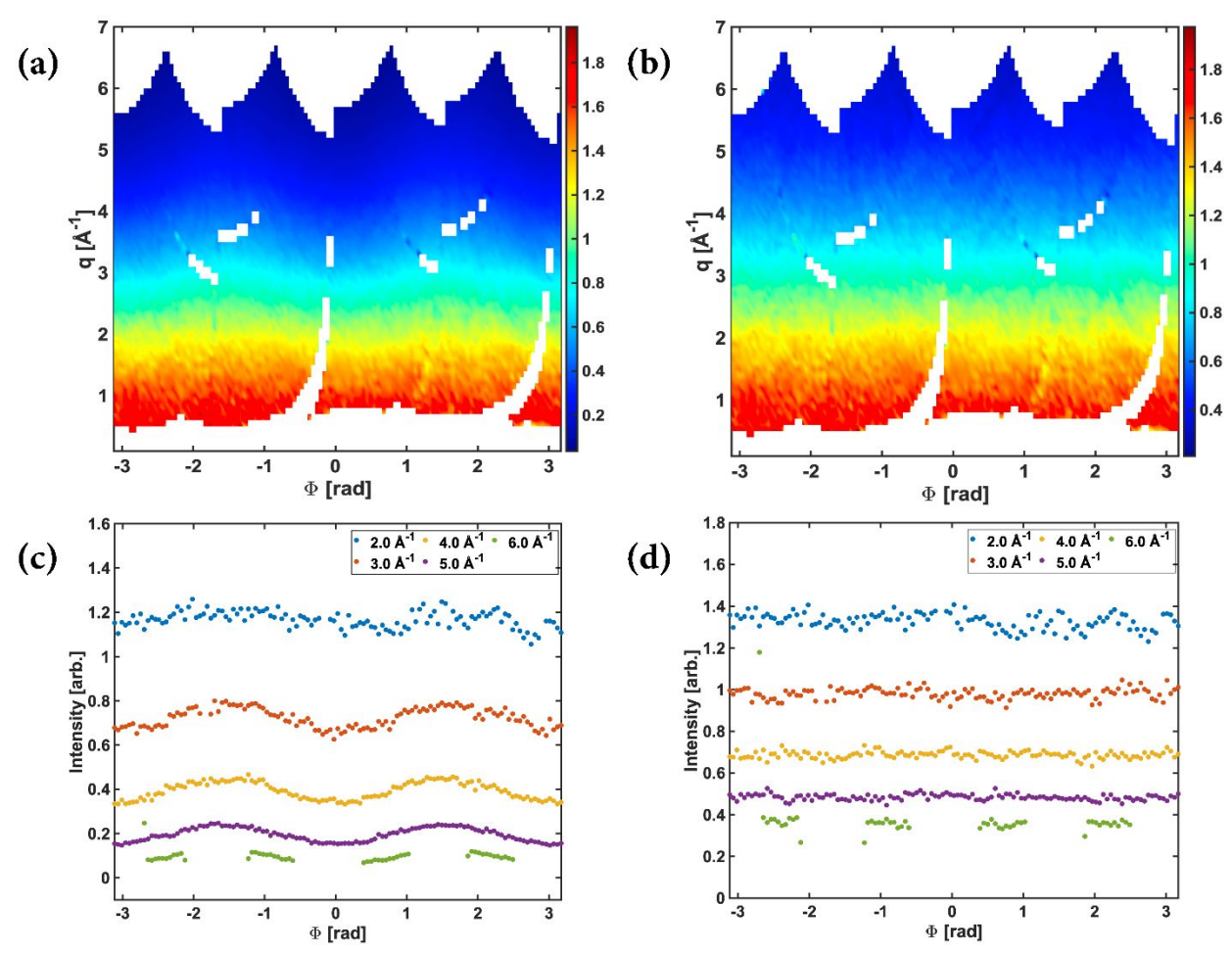


Figure 3: The result of the detector calibration, illustrated on a set of Neon data, obtained by averaging 11064 shots with 15.155 keV X-ray photons. (a) The scattering intensity as measured, in arbitrary units, as a function of the scattering vector, q, and the azimuthal angle, ϕ . Blank areas are either outside the detector range ($q \le \sim 0.5 \text{ Å}^{-1} \text{ & } q \ge 5 \text{ Å}^{-1}$) or blocked out because of artifacts in the detector ($\sim 0.5 \text{ Å}^{-1} < q < 5 \text{ Å}^{-1}$). (b) The scattering intensity after applying geometry and polarization corrections. (c, d) the intensities for selected scattering vectors from (a) and (b), respectively.

Figure 3(a) shows the measured two-dimensional detector image of Neon expressed in scattering vector magnitude q and azimuthal angle ϕ , obtained via Cartesian to polar conversion of the raw scattering image. Neon is chosen as an ideal calibrant gas, given that it is atomic and inert in nature, and possesses a reasonable scattering cross-section with minimal risk for detector saturation, as well as the availability of high-level ab-initio calculations for comparison. For selected scattering vectors, the intensities show a trend (Figure 3(c)) due to the polarization of the incoming X-ray beam and the assumed detector placement. After calibrating the detector distance (Z) and its displacement relative to the X-ray beam (X and Y), the scattering intensities are independent of ϕ for each selected scattering vector magnitude q (Figure 3(b)), with comparative lineouts shown in Figures 3(c) and 3(d). A visual comparison between the measured and theoretically calculated two-dimensional images readily yields approximate values of the detector distance (Z_0), and the relative horizontal and vertical distances (X_0 and Y_0) between the incoming X-ray beam and the

center of the detector. In order to find the optimal values for these parameters, residuals (*Res*) are iteratively calculated as:

$$\begin{split} Res(Z,X_{0},Y_{0}) &= \sum_{q}^{Nq} \sum_{\varphi}^{N_{\varphi}} |I_{\varphi,q}^{\text{corr}}(Z,X_{0},Y_{0}) - I_{\varphi,q}^{\text{avg}}(Z,X_{0},Y_{0})| \\ Res(X,Z^{*},Y_{0}) &= \sum_{q}^{Nq} \sum_{\varphi}^{N_{\varphi}} |I_{\varphi,q}^{\text{corr}}(X,Z^{*},Y_{0}) - I_{\varphi,q}^{\text{avg}}(X,Z^{*},Y_{0})| \\ Res(Y,Z^{*},X^{*}) &= \sum_{q}^{Nq} \sum_{\varphi}^{N_{\varphi}} |I_{\varphi,q}^{\text{corr}}(Y,Z^{*},X^{*}) - I_{\varphi,q}^{\text{avg}}(Y,Z^{*},X^{*})| \end{split}$$

where X^* , Y^* , and Z^* refer to the optimal values; X, Y, and Z are variables being searched for; Nq and N_{φ} are the number of scattering vector q bins and azimuthal angle φ bins; $I_{\varphi,q}^{\text{corr}}$ is the measured scattering intensity at bins q and φ after geometry and polarization correction given the corresponding calibration parameters; and $I_{\varphi,q}^{\text{avg}}$ is the average of the corrected scattering intensity for φ bins under one specific q bin, i.e., $I_{\varphi,q}^{\text{avg}} = \frac{1}{N_{\varphi}} \sum_{\varphi}^{N_{\varphi}} I_{\varphi,q}^{\text{corr}}$. By applying an iterative search for optimal X, Y, and Z values, X^* , Y^* , and Z^* can be found via polynomial fits.

In our experiments, the detector calibration is performed on SF_6 , which scatters strongly and, on account of its highly symmetric structure, has a well-modulated scattering pattern. Importantly, the calibration parameters obtained are independent of any computational model of the scattering signal as a function of scattering vector as they are purely determined from experimental measurements. Nevertheless, the agreement of the experimental with the computed patterns is excellent as shown in Figure 4. For this visual illustration, an IAM pattern was employed.

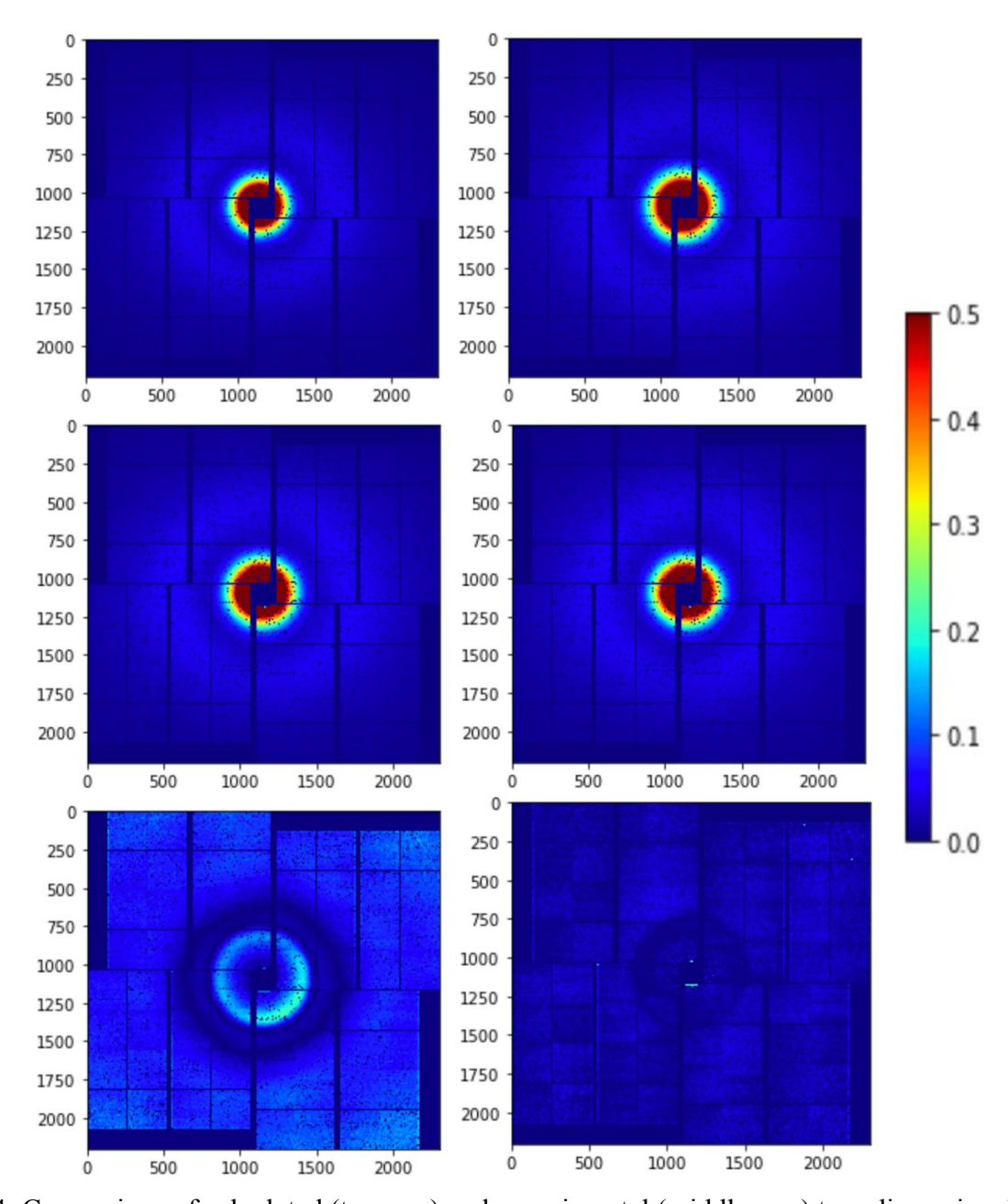


Figure 4: Comparison of calculated (top row) and experimental (middle row) two-dimensional X-ray scattering patterns of the ground-state SF_6 with 15.155 keV X-rays, and the percent difference between them (bottom row). This illustration used an IAM calculation. The left column is before fine calibration of the detector position, and the right column is after. The tiny dark spots on the detector images are bad pixels that had been masked out.

3.2 Angle-of-scattering corrections

To directly compare the experimental scattering pattern I(q) to the theoretical results, a series of calibrations and corrections should be applied. In addition to the detector position calibration and

corrections for the pixel geometry of the detector described above, this includes corrections for the beryllium window, as well as the detector efficiency dependence on the angle-of-incidence. With these corrections, excellent quantitative agreement between experimental data and high-level theoretical calculations can be achieved.

The radially averaged scattering signals, obtained with only the optimized detector positions, the X-ray polarization and the pixel geometry correction accounted for, show systematic deviations in the medium to high *q* range when compared to theoretical patterns from *ab initio* methods. This is illustrated in Figure 5 using a rare gas (neon) and three molecular systems, sulfur hexafluoride (SF₆), quadricyclane (QC, C₇H₈), and norbornadiene (NB, C₇H₈). To reach quantitative agreement between experimental and theoretical scattering patterns, the following angle-of-scattering corrections must be introduced: corrections for the geometry of the scattering sample cell, the transmission of scattered X-rays through the beryllium window of the sample cell, the transmission through the aluminum coating on the detector, the transmission through the Kapton NH/Al protection shielding, and the detection efficiency of silicon of the detector itself. We will discuss each of these factors in turn in the following sections.

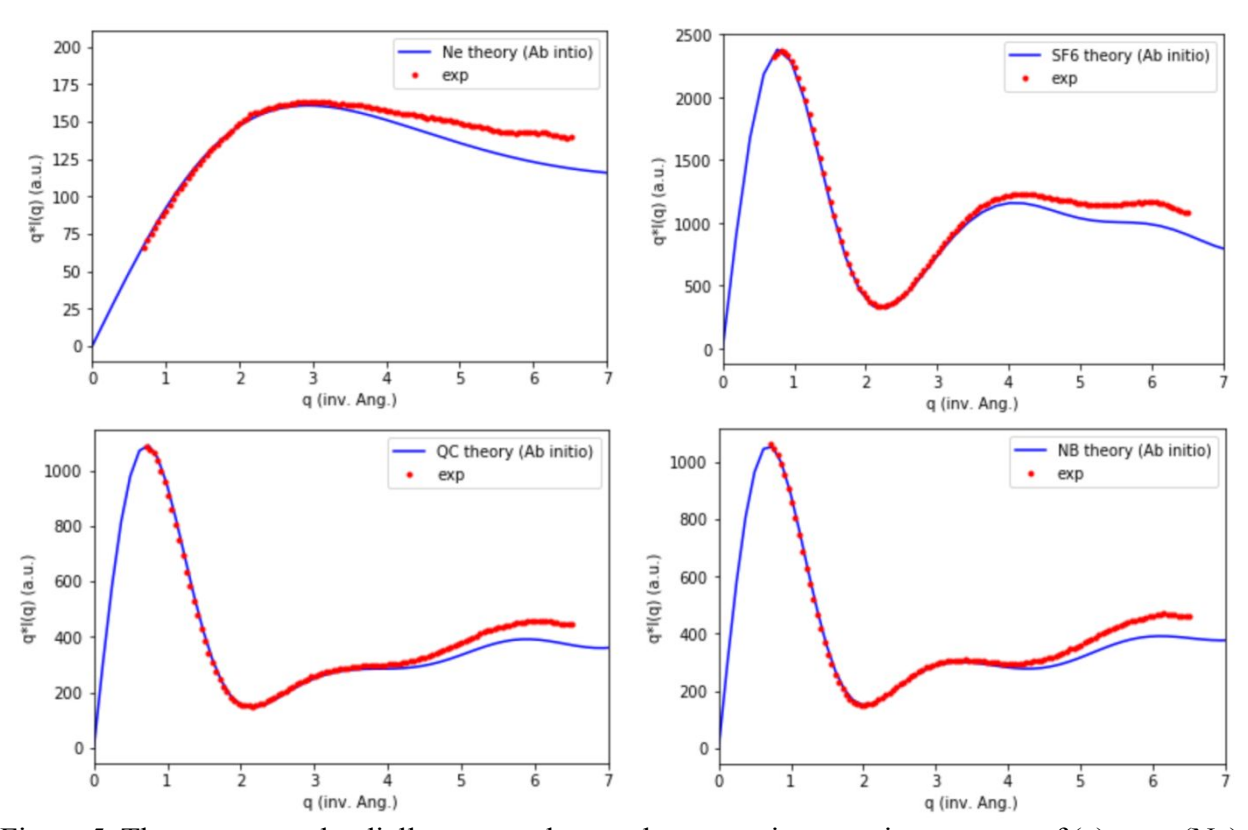


Figure 5: The uncorrected radially averaged ground-state static scattering patterns of (a) neon (Ne), (b) sulfur hexafluoride (SF₆), (c) quadricyclane (QC), and (d) norbornadiene (NB) after detector position calibration and including the correction for X-ray polarization and pixel geometry corrections (as described in section 3.1), measured by 15.155 keV X-rays. There are systematic deviations for all measured systems in the medium to high q range.

3.2.1 Geometry of the scattering cell

Due to the windowless design of the scattering cell, gas can effuse from the holes on either side of the cell. A hole in the beryllium window on the exit side of the cell allows the primary X-ray beam to pass through unperturbed. Scattering from the effusing gas at the exit side can be detected for all q captured by the detector. Therefore, there is no q-dependent correction for effusing gas at the exit side. The effusing gas at the entrance side however, where the X-rays enter the cell through a Pt pinhole, may contribute to the measured scattering signal, particularly at small scattering angles. However, the Pt pinhole blocks the high-q signal as depicted in Figure 6.

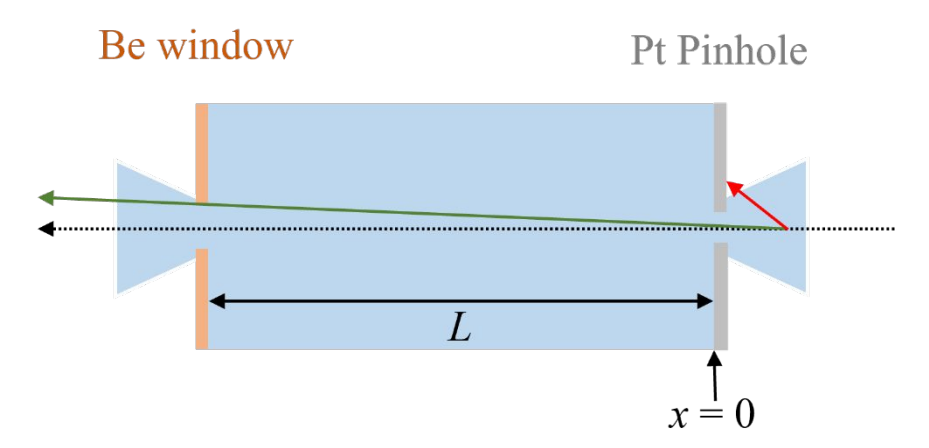


Figure 6: An illustration of the geometry of the scattering cell. The black dotted line represents the primary X-ray beam, which enters through the Pt pinhole on the right and exits through the hole in the Be window to the left. The green solid line represents X-rays scattered from the effusing gas at the entrance side with small scattering angles. The red solid line represents the blocked scattered X-rays with large scattering angles due to the Pt pinhole. *L* is the path length inside the scattering cell.

Pathlength in the Pt pinhole

Assuming the gas density inside the pinhole is equivalent to the main sample cell, there is an additional length given by the thickness of the pinhole, $t_p = 125 \, \mu m$. Assuming that the X-ray beam is centered on the pinhole, the pinhole of radius $r_p = 125 \, \mu m$ limits the additional pathlength $x_p(2\theta)$ inside the pinhole from which the scattering can be detected. Since

$$\tan(2\theta) = \frac{r_p}{-x_p(2\theta)} ,$$

With $x_p \le 0$ defined as it is situated prior to the length of the scattering cell, the extra pathlength from gas inside the pinhole is therefore

$$x_{P}(2\theta) = \begin{cases} -\frac{r_{P}}{\tan(2\theta)} & for \frac{r_{P}}{\tan(2\theta)} \leq t_{P} \\ -t_{P} & for \frac{r_{P}}{\tan(2\theta)} > t_{P} \end{cases}$$

Effective pathlength in the effusing gas upstream of the Pt pinhole

For large scattering angles, i.e., $\tan(2\theta) \ge \frac{r_P}{t_P}$, none of the X-rays scattered from the emanating gas is detected, thus they give no additional contribution to the scattering signal. For small scattering angles, $\tan (2\theta) \le \frac{r_p}{t_p}$, X-rays scattered from the emanating gas may get detected, giving rise to additional scattering signals. Specifically, for any 2θ , the additional scattering signal can be detected up to a distance x_{max} , which is given by

$$\frac{r_P}{t_P - x_{\text{max}}} = tan2\theta$$

Where $x_{\text{max}} \leq 0$ is defined as it is situated prior to the length of the scattering cell. Then,

$$x_{\max} = t_P - \frac{r_P}{\tan 2\theta}$$

In addition, the gas density is decreasing as the gas expands into the vacuum. While more sophisticated gas dynamics calculations could capture the gas density quantitatively, the details will depend on the nature of the gas. Here we assume for simplicity that the gas emerges in a 90° cone, causing the gas density to decrease as the area of the expansion increases. While surely not quantitatively correct, this approximation captures the essence of the small correction term needed.

At the entrance to the pinhole, x = 0, the area is

$$A(0) = \pi \cdot r_p^2$$

 $A(0) = \pi \cdot r_p^2$ Further downstream (prior to the entrance of the scattering cell, $x \le 0$), the area is defined as

$$A(x) = \pi \cdot (r_P - x)^2$$

The density is therefore given by

$$\rho(x) = \rho_0 \cdot \frac{A(0)}{A(x)} = \rho_0 \cdot \frac{(r_P)^2}{(r_P - x)^2}$$

where ρ_0 is the assumed uniform gas density inside the scattering cell.

The signal arising from scattering in the expanding part of the gas is then given by the integral

$$\int_{x_{\text{max}}}^{0} \rho(x) dx = \rho_0 \cdot \frac{r_P \cdot x_{\text{max}}}{x_{\text{max}} - r_P}$$

Combined with $x_{\text{max}} = t_P - \frac{r_P}{\tan(2\theta)}$, this yields the dependence of the signal on the scattering angle.

Combined cell geometry corrections

The total scattering signal scales as the product of the pathlength and gas density. Combining all the contributions, the effective pathlength is

$$L' = L + \begin{cases} \frac{r_P}{\tan(2\theta)} & for \tan(2\theta) \ge \frac{r_P}{t_P} \\ t_P + \frac{r_P \cdot x_{\max}}{x_{\max} - r_P} & for \tan(2\theta) < \frac{r_P}{t_P} \end{cases}$$

Where L is the nominal pathlength inside of the scattering cell and L' is the corrected length accounting for potential scattering en route to the cell.

The correction factor for the geometry of the scattering cell $(\eta_{Cell}(2\theta))$ is defined as

$$\eta_{Cell}(2\theta) = \frac{L'}{L} = \begin{cases} 1 + \frac{1}{L} \cdot \frac{r_P}{\tan(2\theta)} & for \tan(2\theta) \ge \frac{r_P}{t_P} \\ 1 + \frac{1}{L} \cdot \left(t_P + \frac{r_P \cdot x_{\max}}{x_{\max} - r_P}\right) & for \tan(2\theta) < \frac{r_P}{t_P} \end{cases}$$

$$Eq. 3.2.1$$

For the experimental conditions of the scattering cell used in the present experiments, the correction is plotted in Figure 7. It can be seen that the correction amounts to several percent, depending on the scattering angle.

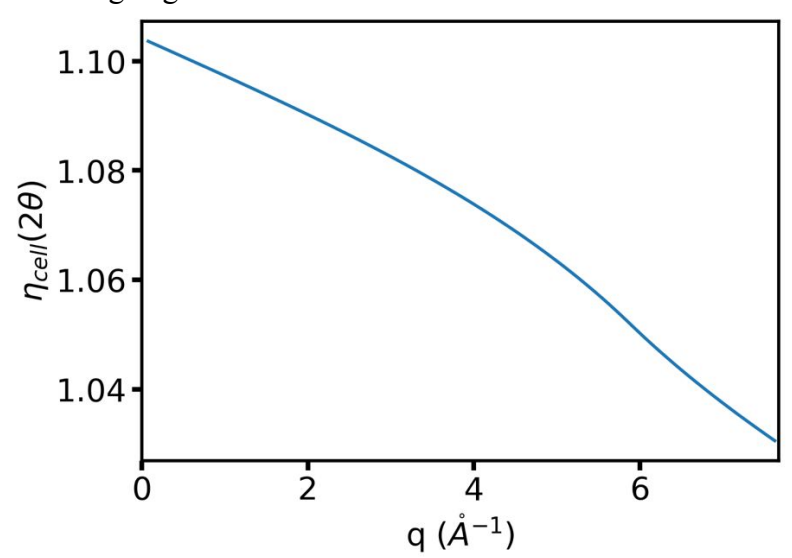


Figure 7: Corrections for the geometry of the scattering cell with the pinhole of radius and thickness $r_p = 125 \,\mu m$, $t_p = 125 \,\mu m$, and the path length inside of the scattering cell $L = 2.4 \,mm$.

3.2.2 Transmission through the beryllium window of the scattering cell

At the exit side of the scattering cell, a hole in the beryllium window transmits the primary X-ray beam. The thickness of the Be window is $x_{Be} = 100 \, \mu m$, and the radius of the hole is 250 μm . The attenuation by the Be window depends on q, because the pathlength of the scattered X-rays through the window varies with the scattering angle. At an angle 2θ

$$x(2\theta) = \frac{x_{Be}}{\cos(2\theta)}$$

where $x(2\theta)$ is the pathlength of the transmitted X-ray beam and x_{Be} is the thickness of the window.

As the scattered X-rays travel through the Be window, they are partially absorbed. The intensity drops exponentially with an absorption length of $x_{Be,0}$. The intensity of the transmitted X-ray beam through a distance x is

$$I(x) = I_0 \cdot e^{-\frac{x}{x_{Be,0}}}$$

 $I(x) = I_0 \cdot e^{-\frac{x}{x_{Be,0}}}$ where I_0 is the intensity of the incoming X-ray beam.

At normal incidence, the pathlength is given by the thickness of Be window, $x_{Be} = 100 \ \mu m$. According to the dataset of Henke⁶²:

$$T = \frac{I}{I_0} = e^{-\frac{x_{Be}}{x_{Be, 0}}}$$

The absorption length with a photon energy of 15.155 keV is $x_{Be,0} = 21,409 \ \mu m$.

The angle-dependent transmission factor of the Be window is

$$T(2\theta) = e^{-\frac{x_{Be}}{x_{Be,0} \cdot \cos(2\theta)}}$$

Due to the $r_h = 250 \,\mu m$ in the Be window, it is possible for part of the scattered X-rays to emerge from the cell directly through the hole in the Be window, while other parts pass through the window and incur attenuation. The relative fractions of each depend on the scattering angle.

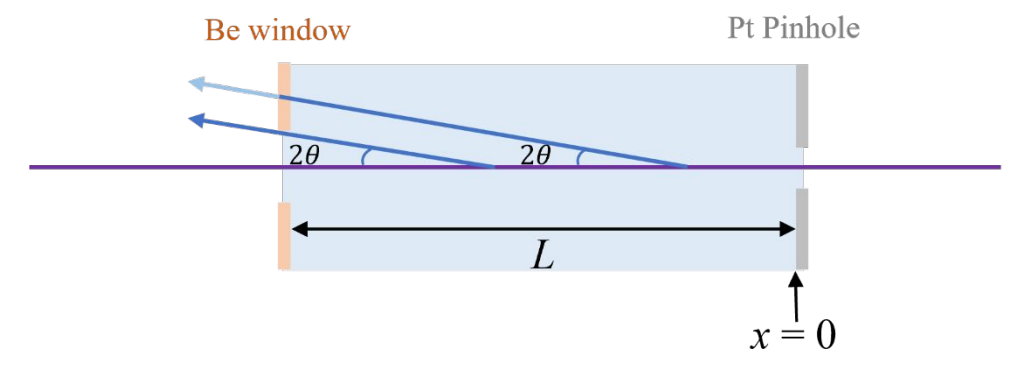


Figure 8: An illustration of the geometry of the scattering cell and transmission through the beryllium window at the exit side.

The pathlength x where scattered X-rays pass through the hole is

$$x(2\theta) = \frac{r_h}{\tan(2\theta)}$$

For small angles, the maximum pathlength
$$x$$
 is equal to the pathlength $L = 2.4$ mm, therefore,
$$x(2\theta) = \begin{cases} \frac{r_h}{\tan(2\theta)} & \text{for } \frac{r_h}{\tan(2\theta)} \leq L \\ L & \text{for } \frac{r_h}{\tan(2\theta)} > L \end{cases}$$

which means $x(2\theta)$ is not larger than L.

A fraction of the pathlength $x(2\theta)$ (i.e., $\frac{x}{L}$) bypasses the Be window, while a fraction $\frac{L-x(2\theta)}{L}$ passes through the Be window and is partially attenuated. The attenuation is the angle-dependent transmission factor $T(2\theta) = e^{-\frac{x_{Be}}{x_{Be,0} \cdot \cos(2\theta)}}$.

The overall correction factor for the Be window is then
$$\eta_{Be}(2\theta) = \frac{x(2\theta)}{L} + \frac{L - x(2\theta)}{L} \cdot e^{-\frac{x_{Be}}{x_{Be,0} \cdot \cos(2\theta)}}$$
Eq. 3.2.2

Using the applicable values of the parameters, the correction for the Be window is dependent on q, but only applies a small correction, as plotted in Figure 9.

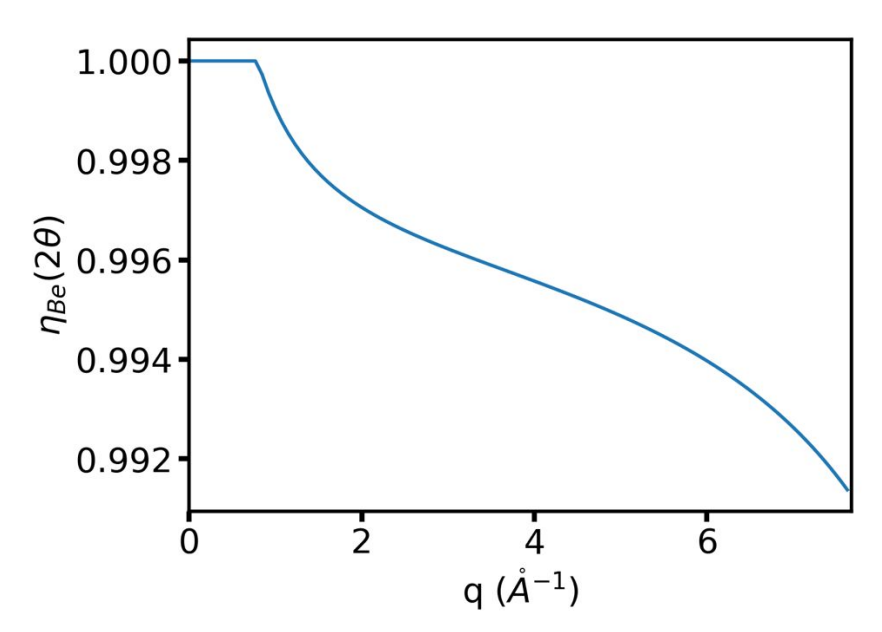


Figure 9: Corrections for the Be window for an X-ray photon energy of 15.155 keV.

3.2.3 Transmission through the aluminum coating on the detector

There is a 3.5 μm thick aluminum coating on the surface of the detector. A similar formula to 3.2.2 can be applied to account for the transmission through the Al coating. According to the dataset of Henke⁶², the absorption length of Al with a photon energy of 15.155 keV is

$$x_{Al.0} = 513 \ \mu m$$

With $x_{Al} = 3.5 \ \mu m$, the angle-dependent transmission factor of the Al coating is

$$T(2\theta) = e^{-\frac{x_{Al}}{x_{Al,0}\cdot\cos(2\theta)}}$$

The correction factor arising from the Al coating is then

$$\eta_{Al}(2\theta) = \frac{T_{Al}(2\theta)}{T_{Al}(2\theta = 0)} = \frac{e^{-\frac{x_{Al}}{x_{Al,0} \cdot \cos(2\theta)}}}{e^{-\frac{x_{Al}}{x_{Al,0}}}}$$
 Eq. 3.2.3

This is plotted in Figure 10. Again, the effect of the aluminum coating is small and will likely only be significant in the most demanding situations.

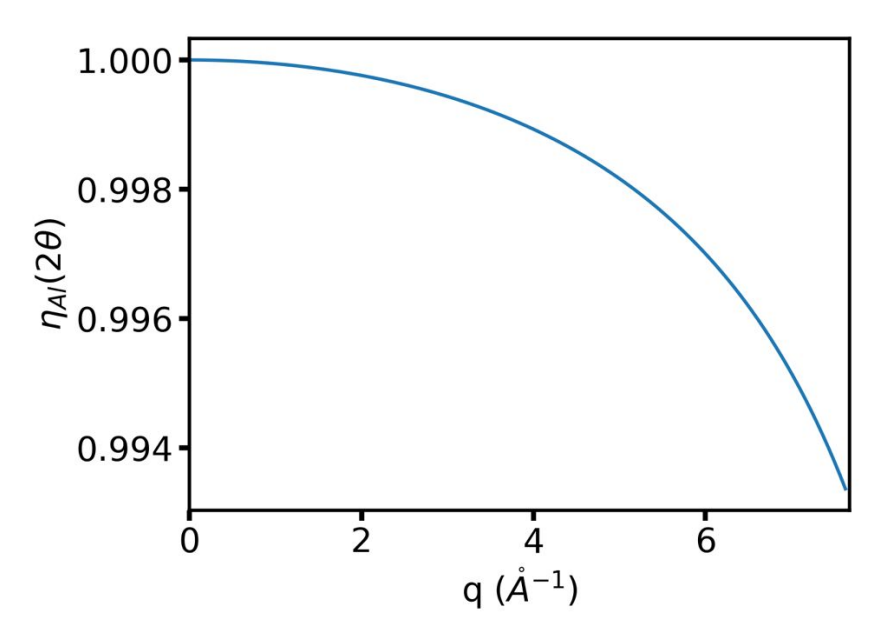


Figure 10: Corrections for the Al coating for an X-ray photon energy of 15.155 keV.

3.2.4 Transmission through the Kapton NH/Al Detector Protection

The Jungfrau 4M detector is protected by an 8 μm thick shield of Kapton NH covered with 1 μm of sputtered aluminum. Since the attenuation arising from the 3.5 μm aluminum coating is small, as discussed in 3.2.3, the attenuation of the 1 μm sputtered aluminum is negligible. For brevity, we therefore focus on the transmission through the 8 μm Kapton NH, which can be treated similarly to the beryllium and aluminum corrections. Based on the dataset of the Henke, the absorption length of Kapton NH with a photon energy of 15.155 keV is

$$x_{Kapton, 0} = 7917 \ \mu m$$

With $x_{Kapton} = 8 \mu m$, the scattering angle-dependent transmission factor of the Kapton NH is

$$T(2\theta) = e^{-\frac{x_{Kapton}}{x_{Kapton,0} \cdot \cos(2\theta)}}$$

The correction factor arising from the Kapton NH is then

$$\eta_{Kapton}(2\theta) = \frac{T_{Kapton}(2\theta)}{T_{Kapton}(2\theta = 0)} = \frac{e^{-\frac{x_{Kapton}}{x_{Kapton}, 0 \cdot \cos(2\theta)}}}{e^{-\frac{x_{Kapton}}{x_{Kapton}, 0}}}$$
 Eq. 3.2.4

This is plotted in Figure 11. The effect of the Kapton NH protective shielding is very small and can be neglected in most cases.

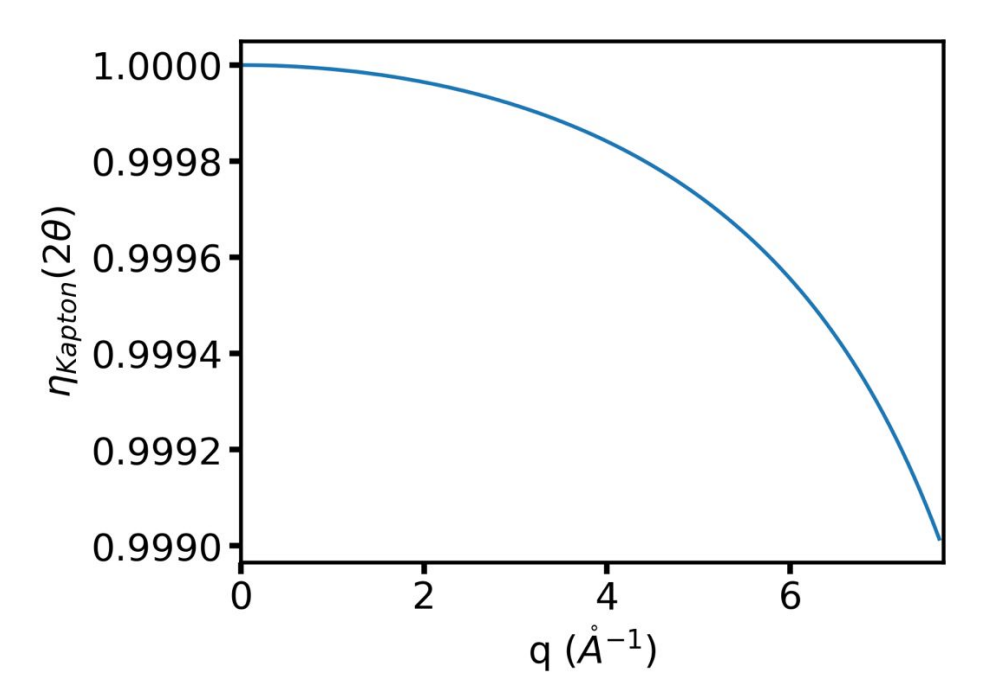


Figure 11: Corrections for the Kapton NH protective shielding for an X-ray photon energy of 15.155 keV.

3.2.5 Detection efficiency of the detector

The thickness of the silicon pixels of the Jungfrau detector is $x_{Si} = 318.5 \ \mu m$. Some of the X-ray photons entering the silicon get absorbed and give rise to the measured signal, while others are transmitted and are not detected. Even very highly doped silicon contains dopants on the order of parts per thousand, a proportion that may be as small as parts per billion in very lightly doped silicon. We therefore treat the silicon of the Jungfrau detector as if it was pure silicon. The formula of the transmitted X-ray intensity in 3.2.2 can also be applied here. Thus, the absorbed intensity of the X-ray beam is

$$I_0 - I(x) = I_0 \cdot \left(1 - e^{-\frac{x}{x_{Si,0}}}\right)$$

 $I_0-I(x)=I_0\cdot \left(1-e^{-\frac{x}{x_{Si,0}}}\right)$ The detection efficiency is defined as the fraction of the beam that is absorbed.

$$\frac{I_0 - I(x)}{I_0} = \left(1 - e^{-\frac{x}{x_{Si,0}}}\right)$$

 $\frac{I_0 - I(x)}{I_0} = \left(1 - e^{-\frac{x}{x_{Si,0}}}\right)$ At normal incidence, the pathlength is given by the pixel depth x_{Si} . The efficiency is therefore

$$\left(1-e^{-\frac{x_{Si}}{x_{Si,0}}}\right)$$

Based on the dataset of Henke⁶², the absorption length of Si at an X-ray photon energy of 15.155 keV is

$$x_{cio} = 456 \, \mu m$$

 $x_{Si,0} = 456 \ \mu m$ At an angle 2θ , the pathlength becomes larger and is

$$x(2\theta) = \frac{x_{Si}}{\cos(2\theta)}$$

Therefore, the detection efficiency at 2θ is

$$\left(1 - e^{-\frac{x_{Si}}{x_{Si,0} \cdot \cos(2\theta)}}\right)$$

The correction for the transmission through the silicon of the detector, i.e., the change in the detection efficiency with scattering angle, is defined as

$$\eta_{Si}(2\theta) = \frac{1 - e^{-\frac{x_{Si}}{x_{Si,0} \cdot \cos(2\theta)}}}{1 - e^{-\frac{x_{Si}}{x_{Si,0}}}} \qquad Eq. \ 3.2.5$$
The parameters the angle-dependent definition of the state of

With the applicable values of all parameters, the angle-dependent detection efficiency of the silicon detector is as shown in Figure 12. It is apparent that this correction factor makes an important contribution.

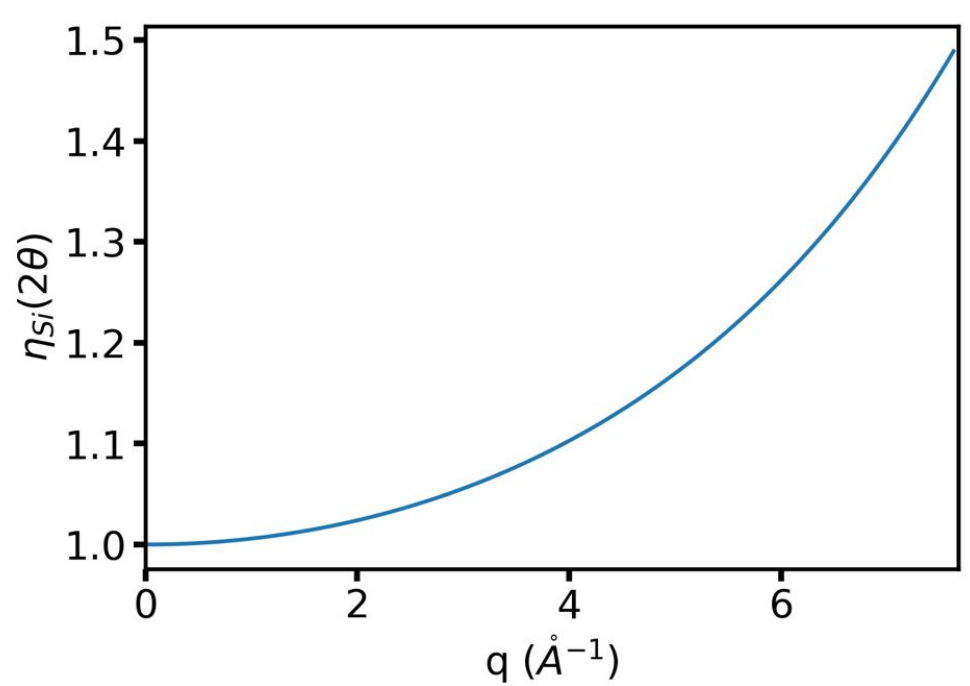


Figure 12: Corrections for the transmission through the silicon of the detector, for an X-ray photon energy of 15.155 keV.

3.2.6 Combined angle-of-scattering corrections

Combining all these factors, the angle-of-scattering (AoS) corrections are given by

$$\eta_{AoS}(2\theta) = \eta_{Cell}(2\theta) \cdot \eta_{Be}(2\theta) \cdot \eta_{Al}(2\theta) \cdot \eta_{Kapton}(2\theta) \cdot \eta_{Si}(2\theta) \qquad Eq. 3.2.6$$

With the individual terms as given in Eq. 3.2.1, 3.2.2, 3.2.3, 3.2.4, 3.2.5. To include these corrections, the raw data needs to be divided by this correction factor.

The angle-of-scattering correction depends on the X-ray photon energy as the absorption lengths of silicon, beryllium, aluminum, and Kapton NH change with the X-ray photon energy. Table 1 shows the absorption length of *Si*, *Be*, *Al*, and Kapton NH at X-ray photon energies of 10, 15, 18, and 20 keV⁶². Clearly, these absorption lengths vary significantly over the photon energy ranges typically used in gas phase X-ray scattering experiments.

Table 1: The absorption lengths (μm) of silicon, beryllium, aluminum, and Kapton NH at different X-ray photon energies.

	10 keV	15 keV	18 keV	20 keV
Si	134	443	760	1038
Be	9593	21092	25992	28199
Al	150	498	856	1169
Kapton	2349	7688	12304	15381

The variable absorption lengths give rise to angle-of-scattering corrections for different X-ray photon energies as shown in Figure 13. Due to the effusing gas at the entrance side of the scattering sample cell, which contributes additional measured scattering signal especially at the low q range, all angle-of-scattering corrections in Figure 13 start with a correction value around 1.1 rather than 1.

The angle-of-scattering corrections are especially pronounced for harder X-rays, with a trend observed for photon energies of 15 keV, 18 keV and 20 keV, which are dominated by angle-of-scattering dependent absorptions within the silicon detector. As the X-ray photon energy is increased, the energy-dependent absorption length within silicon becomes longer, resulting in increased transmission through the Jungfrau detector. Additionally, as a result of the longer geometrical path length through the silicon pixels with increasing scattering angle, the probability of photon absorption is observed to be higher at larger values of q. This combination of effects leads to an overall correction with a pronounced upwards trend with increasing q. Interestingly, for 10 keV photons, the angle-of-scattering correction is almost independent of the angle. This is because the Si absorption length at 10 keV is 134 μm , which is less than the thickness of the pixels on the detector (318.5 μm). Therefore, the detector measures the scattered X-ray photons efficiently for all scattering angles. The angle-of-scattering correction at 10 keV is then dominated by the geometry of the scattering cell, leading to a slightly decreasing correction term with increasing scattering vector.

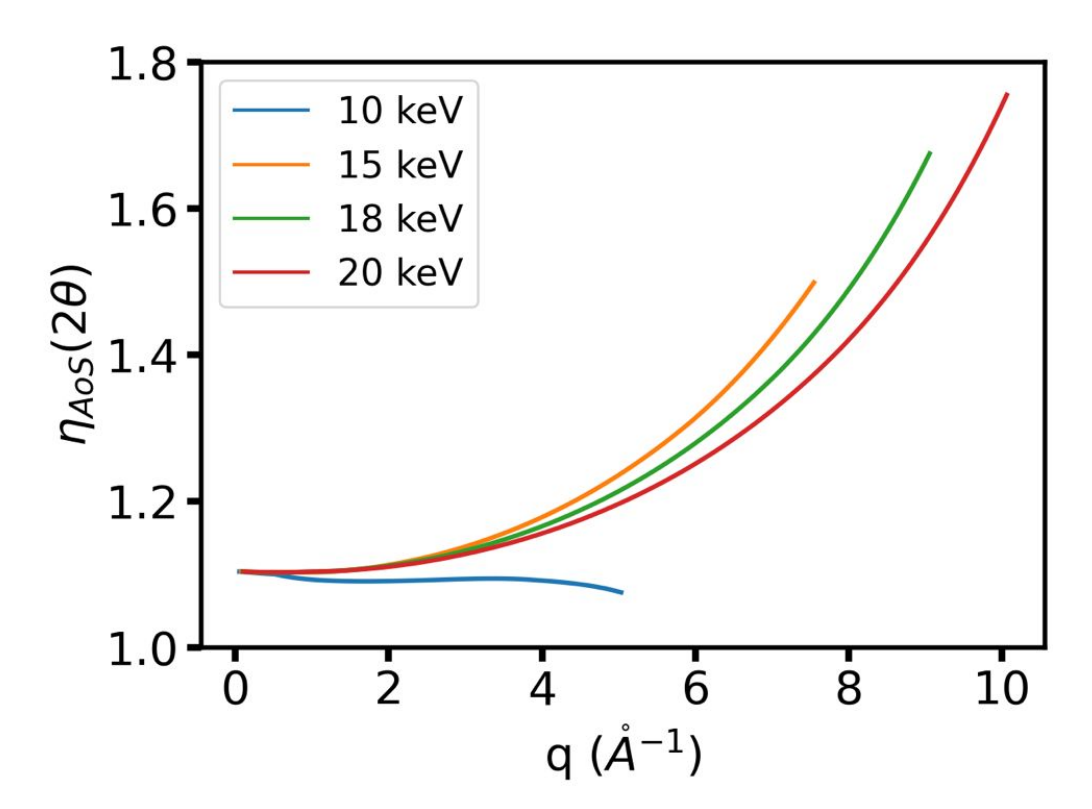


Figure 13: The combined angle-of-scattering corrections, $\eta_{AoS}(2\theta)$, for X-ray photon energies of 10, 15, 18, and 20 keV.

3.3 The detector sensitivity correction matrix

In order to correctly report the number of scattered photons on each pixel of the Jungfrau 4M detector, the manufacturer of the detector measured the instrument response for each pixel on the detector, as shown in Figure 14. At present, only seven out of the eight tiles have been calibrated. This measurement was performed on each tile by creating a histogram of the pixel response value (registered in Analog-to-Digital Units, ADU) across the tile over an adequate number of X-ray shots. Through the analysis of the pixel response, the averaged ADU value per photon was determined. Similarly, the measured total scattering signal (in ADU) can be further calibrated by dividing by the manufacturer correction matrix to provide an estimate of the number of scattered photons collected by each pixel of the Jungfrau 4M detector.

Due to the lack of correction information for the left-most tile on the bottom row, in the present study we only applied the 7-tile manufacturer correction matrix to the measured scattering patterns.

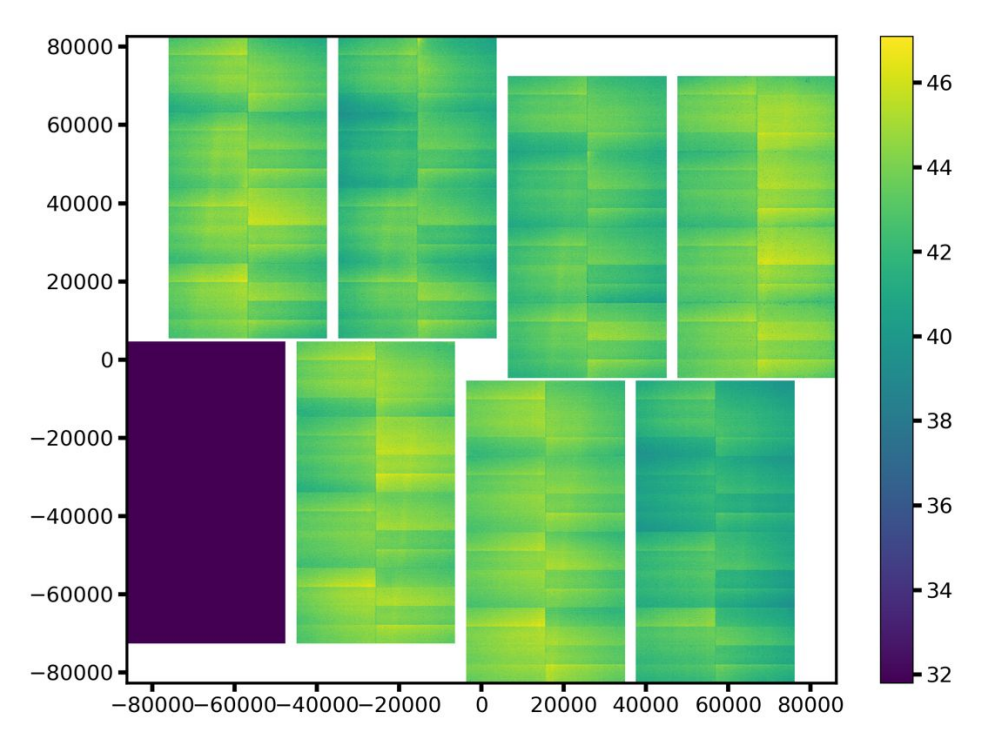


Figure 14: The manufacturer correction matrix for the Jungfrau 4M detector.

4. Implementation

Implementing the detector position calibration, the correction for the X-ray polarization, the pixel geometry correction, the detector sensitivity correction matrix, and the angle-of-scattering corrections, the radially averaged ground-state static scattering signals of model systems quadricyclane and norbornadiene leads to excellent agreement with the computed patterns, as shown in Figure 15. The systematic deviations in the medium to high q range that were present in Figure 5, are now adequately corrected for.

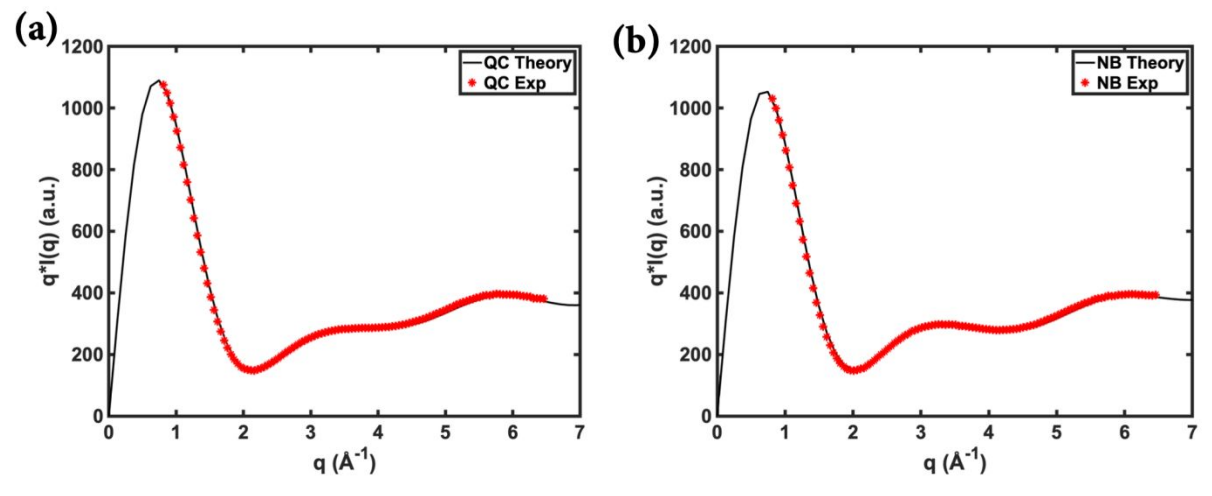


Figure 15: The radially averaged ground-state static scattering pattern of (a) QC, and (b) NB after detector position calibration and including the correction for X-ray polarization, the pixel geometry

correction, the detector sensitivity correction matrix, and the angle-of-scattering corrections, measured with 15.155 keV X-rays. The systematic deviations from the medium to high q seen in Figure 5 are appropriately accounted for. (Data from beamtime LW11.)

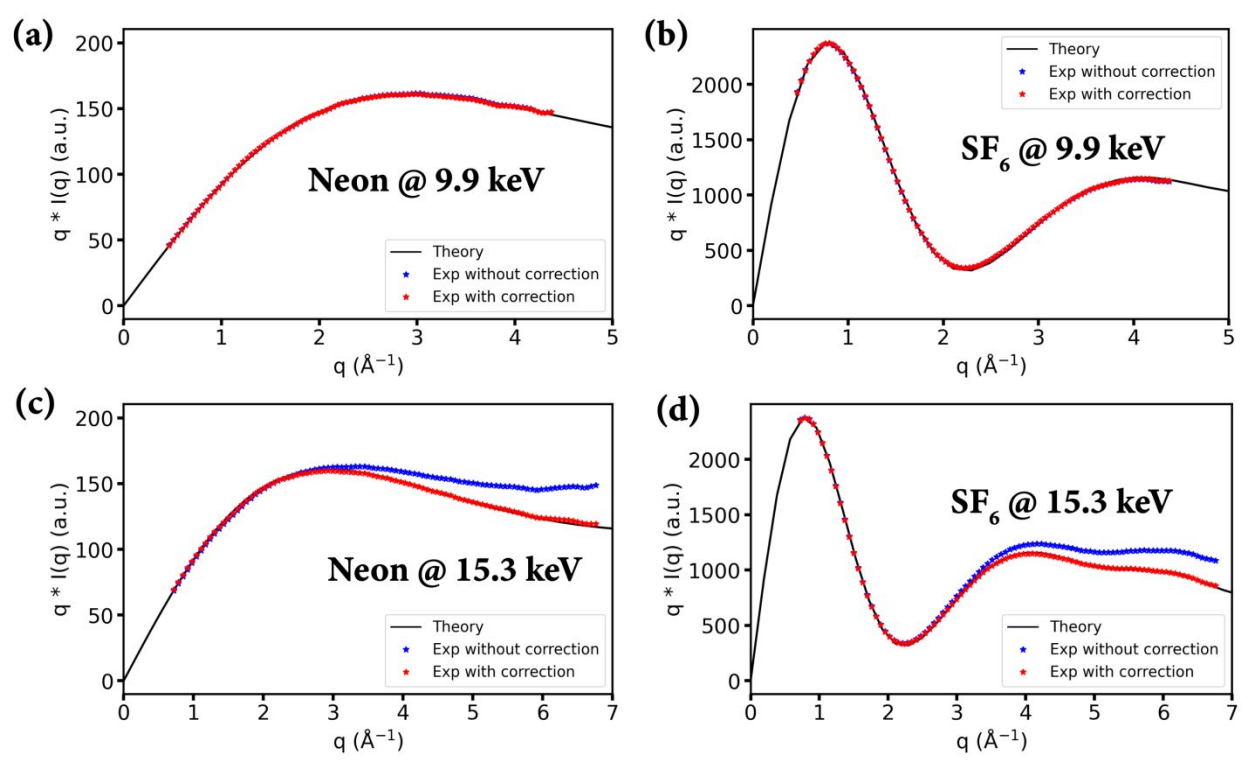


Figure 16: The radially averaged ground-state static scattering patterns of (a, c) Neon, (b, d) SF₆ at X-ray photon energies of 9.9 keV (a, b) and 15.3 keV (c, d), after detector position calibration and the correction for X-ray polarization, the pixel geometry correction, the detector sensitivity correction matrix, and with or without the angle-of-scattering corrections, respectively. (Data from beamtime L10160).

To test the effectiveness of the X-ray photon-energy dependent angle-of-scattering corrections, Figure 16 shows the radially averaged ground-state static scattering patterns of Neon (a, c) and SF₆ (b, d) at X-ray photon energies of 9.9 keV (a, b) and 15.3 keV (c, d) after detector position calibration and the correction for X-ray polarization, the pixel geometry correction, the detector sensitivity correction matrix, and with or without the angle-of-scattering corrections at 9.9 keV and 15.3 keV, respectively. As is already foreshadowed by Figure 13, for 9.9 keV photons the angle-of-scattering corrections are very small across the accessible *q* range, so that implementation of the corrections may be deemed unnecessary. For the higher X-ray photon energies, however, the angle-of-scattering correction are necessary to quantitatively reproduce the computed scattering signals. Their implementation yields a satisfactory agreement between the experimental data and the computed results.

5. Conclusion

X-ray scattering of free molecules in the gas phase provides quantitative measures of electron density distributions in molecular systems, which is immensely useful for measurements of chemical reaction dynamics and kinetics. The determination of excited state structures depends on the accurate knowledge of the ground state structures of the reacting systems. With careful calibration, X-ray scattering experiments can provide these ground state structures.

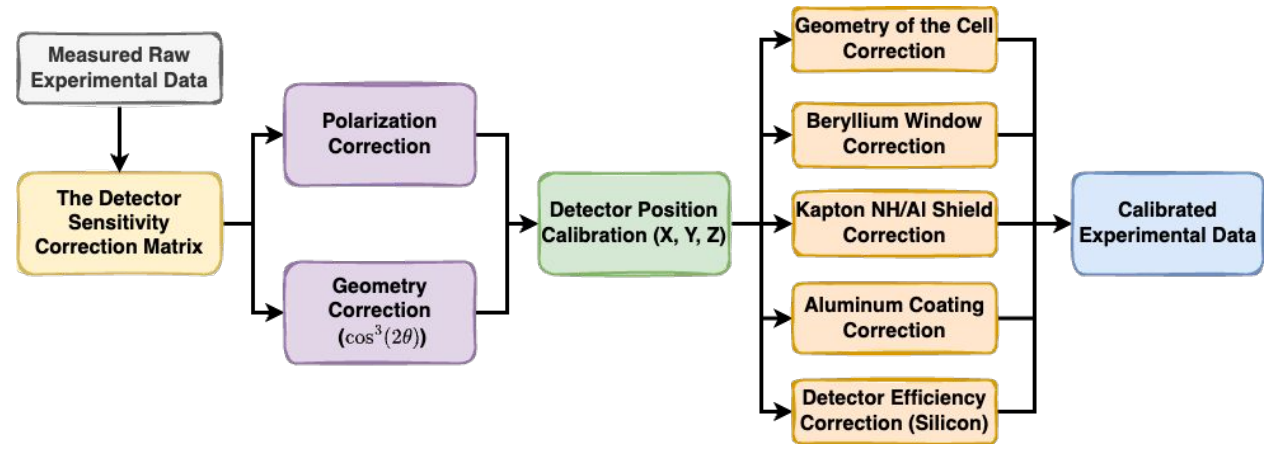


Figure 17: The flowchart of the overall experimental data calibration steps.

We describe a series of calibration steps for gas-phase X-ray scattering experiments and implement them using static, ground-state scattering patterns for a selection of molecules as summarized in Figure 17. Excellent quantitative agreement between experimental measurements and high-level theoretical calculations is achieved. We introduce an experimental pattern self-calibration algorithm to find the optimal detector position that is based on the polarization of the X-rays. By minimizing residuals in an iterative search, the final detector position can be found via polynomial fits. With this calibration algorithm, the geometry of the experiment, particularly the detector distance, can be determined without reference to a theoretical calculation.

To achieve quantitative agreement of the scattering signals between experiment and theory, it is essential to include several angle-of-scattering corrections. These corrections take on increasing importance for higher photon energies. Important corrections include the geometry of the scattering sample cell, the transmission through the beryllium window at the exit side of the cell, the transmission through the aluminum coating on the detector, and the detection efficiency of the silicon detector. The last three of these corrections depend on the photon-energy due to the different absorption lengths of materials at different photon energies. We note that the increased detector efficiency at large scattering vectors is quite helpful since the scattering signals typically decrease for high q.

To further improve the quantitative agreement between experiment and theory, a detection efficiency correction matrix measured by the manufacturer can be implemented. It could also be interesting to explore how elastic and inelastic scattering from the beryllium window might alter the *q*-dependence of the scattering patterns, especially if thicker windows were used. Beyond that, accurate measurements might use scattering from a noble gas to further calibrate the experiment. The quantitative measurement of X-ray scattering signals from free molecules will undoubtedly lead to further exciting insights into ultrafast photochemical reaction dynamics.

Acknowledgements

This project was supported by the National Science Foundation under award # CHE-1953839. NG and LH were funded by the U.S. Department of Energy, Office of Science, Basic Energy Sciences, under award number DE-SC0017995 while SWC was supported by the U.S. Department of Energy, Office of Science, Basic Energy Sciences, under award number DE-SC0020276. NG was supported, in part, by the U.S. Department of Energy, Office of Science, Office of Workforce Development for Teachers and Scientists, Office of Science Graduate Student Research (SCGSR) program. TJAW, AEG, and PL were supported by the AMOS program within the U.S. Department of Energy, Office of Science, Basic Energy Sciences, Chemical Sciences, Geosciences, and Biosciences Division. AEG was funded by the European Union under the project 101067645. The Linac Coherent Light Source, SLAC National Accelerator Laboratory, is supported by the US Department of Energy, Office of Science, Office of Basic Energy Sciences, under contract DE-AC02-76SF00515.

References

¹ Guinier, André. *X-ray diffraction in crystals, imperfect crystals, and amorphous bodies*. Courier Corporation, 1994.

² Henderson, Richard. "The potential and limitations of neutrons, electrons and X-rays for atomic resolution microscopy of unstained biological molecules." *Quarterly reviews of biophysics* 28.2 (1995): 171-193.

³ Hargittai, M., ed. *Stereochemical Applications of Gas-Phase Electron Diffraction, Part A.* Vol. 4. John Wiley & Sons, 1988.

⁴ Zewail, Ahmed H. "Femtochemistry: atomic-scale dynamics of the chemical bond using ultrafast lasers (Nobel Lecture)." *Angewandte Chemie International Edition* 39.15 (2000): 2586-2631.

⁵ Pemberton, Christine C., et al. "From the (1B) spectroscopic state to the photochemical product of the ultrafast ring-opening of 1, 3-cyclohexadiene: a spectral observation of the complete reaction path." *The Journal of Physical Chemistry A* 119.33 (2015): 8832-8845.

⁶ Bühler, Christine C., et al. "Ultrafast dynamics of 1, 3-cyclohexadiene in highly excited states." *Journal of Atomic and Molecular Physics* 2011 (2011).

⁷ Deb, Sanghamitra, and Peter M. Weber. "The ultrafast pathway of photon-induced electrocyclic ring-opening reactions: the case of 1, 3-cyclohexadiene." *Annual review of physical chemistry* 62 (2011): 19-39.

⁸ Rudakov, Fedor, and Peter M. Weber. "Ultrafast structural and isomerization dynamics in the Rydberg-exited Quadricyclane: Norbornadiene system." *The Journal of chemical physics* 136.13 (2012).

⁹ Attar, Andrew R., et al. "Femtosecond x-ray spectroscopy of an electrocyclic ring-opening reaction." *Science* 356.6333 (2017): 54-59.

¹⁰ Larsen, Martin AB, et al. "Putting the Disulfide Bridge at Risk: How UV-C Radiation Leads to Ultrafast Rupture of the S-S Bond." *ChemPhysChem* 19.21 (2018): 2829-2834.

¹¹ Drescher, Markus, et al. "Time-resolved atomic inner-shell spectroscopy." *Nature* 419.6909 (2002): 803-807.

- ¹² Yong, H., A. Kirrander, and P. M. Weber. "Time-resolved x-ray scattering of excited state structure and dynamics." (2023).
- ¹³ Odate, Asami, et al. "Brighter, faster, stronger: ultrafast scattering of free molecules." *Advances in Physics: X* 8.1 (2023): 2126796.
- ¹⁴ Stankus, Brian, et al. "Advances in ultrafast gas-phase x-ray scattering." *Journal of Physics B: Atomic, Molecular and Optical Physics* 53.23 (2020): 234004.
- ¹⁵ Cheng, Xinxin, et al. "Charge localization in a diamine cation provides a test of energy functionals and self-interaction correction." *Nature communications* 7.1 (2016): 11013.
- 16 Cheng, X., Jónsson, E., Jónsson, H. et al. Reply to: "The diamine cation is not a chemical example where density functional theory fails". Nat Commun 9, 5348 (2018).
- ¹⁷ Tudorovskaya, Maria, Russell S. Minns, and Adam Kirrander. "Effects of probe energy and competing pathways on time-resolved photoelectron spectroscopy: the ring-opening of 1, 3-cyclohexadiene." *Physical Chemistry Chemical Physics* 20.26 (2018): 17714-17726.
- ¹⁸ Gosselin, Jaimie L., and Peter M. Weber. "Rydberg fingerprint spectroscopy: a new spectroscopic tool with local and global structural sensitivity." *The Journal of Physical Chemistry A* 109.22 (2005): 4899-4904.
- ¹⁹ Kuthirummal, Narayanan, and Peter M. Weber. "Structure sensitive photoionization via Rydberg levels." *Journal of Molecular Structure* 787.1-3 (2006): 163-166.
- ²⁰ Minitti, Michael P., and Peter M. Weber. "Time-resolved conformational dynamics in hydrocarbon chains." *Physical review letters* 98.25 (2007): 253004.
- ²¹ Deb, Sanghamitra, et al. "Structural dynamics in floppy systems: Ultrafast conformeric motions in Rydberg-excited triethylamine." *The Journal of Physical Chemistry A* 115.10 (2011): 1804-1809.
- ²² Williamson, S., Gérard Mourou, and James CM Li. "Time-resolved, laser-induced phase transformation in aluminum." *MRS Online Proceedings Library* 35 (1984): 87-96.
- ²³ Thompson, John R., Peter M. Weber, and Peder J. Estrup. "Pump-probe low-energy electron diffraction." *Time-Resolved Electron and X-Ray Diffraction*. Vol. 2521. SPIE, 1995.
- ²⁴ Geiser, Joseph D., and Peter M. Weber. "High-repetition-rate time-resolved gas phase electron diffraction." *Time-ResolVed Electron and X-ray Diffraction*. Vol. 2521. SPIE, 1995.
- ²⁵ Elsayed-Ali, Hani E., and Peter M. Weber. "Time-resolved surface electron diffraction." *Time-Resolved Diffraction* (1997): 284-323.
- ²⁶ Hastings, J. B., et al. "Ultrafast time-resolved electron diffraction with megavolt electron beams." *Applied physics letters* 89.18 (2006).
- ²⁷ Dudek, Ray C., and Peter M. Weber. "Ultrafast diffraction imaging of the electrocyclic ring-opening reaction of 1, 3-cyclohexadiene." *The Journal of Physical Chemistry A* 105.17 (2001): 4167-4171.
- ²⁸ Ruan, Chong-Yu, et al. "Ultrafast diffraction and structural dynamics: The nature of complex molecules far from equilibrium." *Proceedings of the National Academy of Sciences* 98.13 (2001): 7117-7122.
- ²⁹ Chergui, Majed, and Ahmed H. Zewail. "Electron and X-Ray Methods of Ultrafast Structural Dynamics: Advances and Applications." *ChemPhysChem* 10.1 (2009): 28-43.

- ³⁰ Miller, RJ Dwayne. "Femtosecond crystallography with ultrabright electrons and x-rays: Capturing chemistry in action." *Science* 343.6175 (2014): 1108-1116.
- ³¹ Siwick, Bradley J., et al. "An atomic-level view of melting using femtosecond electron diffraction." *Science* 302.5649 (2003): 1382-1385.
- ³² Zandi, Omid, et al. "High current table-top setup for femtosecond gas electron diffraction." *Structural Dynamics* 4.4 (2017).
- ³³ Cardoza, Job D., et al. "Centering of ultrafast time-resolved pump–probe electron diffraction patterns." *Chemical physics* 299.2-3 (2004): 307-312.
- ³⁴ King, Wayne E., et al. "Ultrafast electron microscopy in materials science, biology, and chemistry." *Journal of Applied Physics* 97.11 (2005).
- ³⁵ Emma, Paul, et al. "First lasing and operation of an ångstrom-wavelength free-electron laser." *nature photonics* 4.9 (2010): 641-647.
- ³⁶ Ishikawa, Tetsuya, et al. "A compact X-ray free-electron laser emitting in the sub-ångström region." *nature photonics* 6.8 (2012): 540-544.
- ³⁷ Weathersby, S. P., et al. "Mega-electron-volt ultrafast electron diffraction at SLAC National Accelerator Laboratory." *Review of Scientific Instruments* 86.7 (2015).
- ³⁸ Minitti, M. P., et al. "Imaging molecular motion: Femtosecond x-ray scattering of an electrocyclic chemical reaction." *Physical review letters* 114.25 (2015): 255501.
- ³⁹ Wolf, Thomas JA, et al. "The photochemical ring-opening of 1, 3-cyclohexadiene imaged by ultrafast electron diffraction." *Nature chemistry* 11.6 (2019): 504-509.
- ⁴⁰ Yong, Haiwang, et al. "Determining orientations of optical transition dipole moments using ultrafast x-ray scattering," *The Journal of Physical Chemistry Letters* 9.22 (2018): 6556-6562.
- ⁴¹ Yong, Haiwang, et al. "Observation of the molecular response to light upon photoexcitation." *Nature communications* 11.1 (2020): 2157.
- ⁴² Yang, Jie, et al. "Simultaneous observation of nuclear and electronic dynamics by ultrafast electron diffraction." *Science* 368.6493 (2020): 885-889.
- ⁴³ Stankus, Brian, et al. "Ultrafast X-ray scattering reveals vibrational coherence following Rydberg excitation." *Nature chemistry* 11.8 (2019): 716-721.
- ⁴⁴ Glownia, J. M., et al. "Self-referenced coherent diffraction x-ray movie of Ångstrom-and femtosecond-scale atomic motion." *Physical review letters* 117.15 (2016): 153003.
- ⁴⁵ Bucksbaum, Philip H., et al. "Characterizing multiphoton excitation using time-resolved x-ray scattering." *Physical Review X* 10.1 (2020): 011065.
- ⁴⁶ Ischenko, Anatoly A., Peter M. Weber, and RJ Dwayne Miller. "Capturing chemistry in action with electrons: realization of atomically resolved reaction dynamics." *Chemical reviews* 117.16 (2017): 11066-11124.
- ⁴⁷ Yang, Jie, et al. "Imaging CF3I conical intersection and photodissociation dynamics with ultrafast electron diffraction." *Science* 361.6397 (2018): 64-67.

- ⁴⁸ Jiang, Yifeng, et al. "Direct observation of nuclear reorganization driven by ultrafast spin transitions." *Nature Communications* 11.1 (2020): 1530.
- ⁴⁹ Ruddock, Jennifer M., et al. "Simplicity beneath complexity: Counting molecular electrons reveals transients and kinetics of photodissociation reactions." *Angewandte Chemie* 131.19 (2019): 6437-6441.
- ⁵⁰ Ruddock, Jennifer M., et al. "A deep UV trigger for ground-state ring-opening dynamics of 1, 3-cyclohexadiene." *Science advances* 5.9 (2019): eaax6625.
- ⁵¹ Waller, I. T., and Douglas Rayner Hartree. "On the intensity of total scattering of X-rays." *Proceedings of the Royal Society of London. Series A, Containing Papers of a Mathematical and Physical Character* 124.793 (1929): 119-142.
- ⁵² Thakkar, Ajit J., A. N. Tripathi, and Vedene H. Smith Jr. "Molecular x-ray-and electron-scattering intensities." *Physical Review A* 29.3 (1984): 1108.
- ⁵³ Bartell, L. S., and R. M. Gavin. "Effects of electron correlation in X-ray and electron diffraction." *Journal of the American Chemical Society* 86.17 (1964): 3493-3498.
- ⁵⁴ Budarz, J. M., et al. "Observation of femtosecond molecular dynamics via pump–probe gas phase x-ray scattering." *Journal of Physics B: Atomic, Molecular and Optical Physics* 49.3 (2016): 034001.
- ⁵⁵ Northey, Thomas, Nikola Zotev, and Adam Kirrander. "Ab initio calculation of molecular diffraction." *Journal of Chemical Theory and Computation* 10.11 (2014): 4911-4920.
- ⁵⁶ Northey, Thomas, et al. "Elastic X-ray scattering from state-selected molecules." *The Journal of Chemical Physics* 145.15 (2016).
- ⁵⁷ Carrascosa, Andrés Moreno, Thomas Northey, and Adam Kirrander. "Imaging rotations and vibrations in polyatomic molecules with X-ray scattering." *Physical Chemistry Chemical Physics* 19.11 (2017): 7853-7863.
- ⁵⁸ Carrascosa, Andrés Moreno, and Adam Kirrander. "Ab initio calculation of inelastic scattering." *Physical Chemistry Chemical Physics* 19.30 (2017): 19545-19553.
- ⁵⁹ Werner, H.-J.; Knowles, P. J.; Knizia, G.; Manby, F. R.; Schütz, M. and others. "MOLPRO, version 2012.1, a package of ab initio programs." See http://www. molpro. net (2012).
- ⁶⁰ Northey, Thomas, Adam Kirrander, and Peter M. Weber. "Extracting the electronic structure signal from X-ray and electron scattering in the gas phase." *Journal of Synchrotron Radiation* 31.2 (2024).
- ⁶¹ Warren, Bertram Eugene. X-ray Diffraction. Courier Corporation, 1990.
- ⁶² B.L. Henke, E.M. Gullikson, and J.C. Davis. *X-ray interactions: photoabsorption, scattering, transmission, and reflection at E=50-30000 eV, Z=1-92*, Atomic Data and Nuclear Data Tables Vol. **54** (no.2), 181-342 (July 1993).